ACS OMEGA

http://pubs.acs.org/journal/acsodf

Article

Electronic and Near-Infrared-II Optical Properties of I-Doped Monolayer $MoTe_2$: A First-Principles Study

Yue Zhao, Ling Liu,* Shuangjie Liu, Yang Wang, Yonghui Li,* and Xiao-Dong Zhang*

Cite This: *ACS Omega* 2022, 7, 11956−11963

Read Online

ACCESS | Metrics & More | Article Recommendations | Supporting Information

ABSTRACT: Near-infrared-II (NIR-II, 1000−1700 nm) fluorescence imaging is widely used for in vivo biological imaging. With the unique electronic structures and capability of band-gap engineering, two-dimensional (2D) materials can be potential candidates for NIR-II imaging. Herein, a theoretical investigation of the electronic structure and optical properties of iodine (I)-doped monolayer $MoTe_2$ systems with different doping concentrations is carried out through simulations to explore their NIR optical properties. The results suggest that the emergence of impurity levels due to I doping effectively reduces the bandwidth of I-doped monolayer $MoTe_2$ systems, and the bandwidth decreases with the increase in the I doping concentration. Although the I and Mo atoms possess clear covalent-bonding features according to the charge density difference, impurity levels induced by the strong hybridization between the I 5p and Mo 4d orbitals cross the Fermi level, making the doped systems exhibit metallic behavior. In addition, with the increase in the I doping concentration, the energy required for electron transition from valence bands to impurity levels gradually decreases, which can be linked to the enhancement of the optical absorption in the red-shifted NIR-II region. Meanwhile, with a higher I doping concentration, the emission spectra, which are the product of the absorption spectra and quasi-Fermi distributions for electrons and holes, can be enhanced in the NIR-II window.

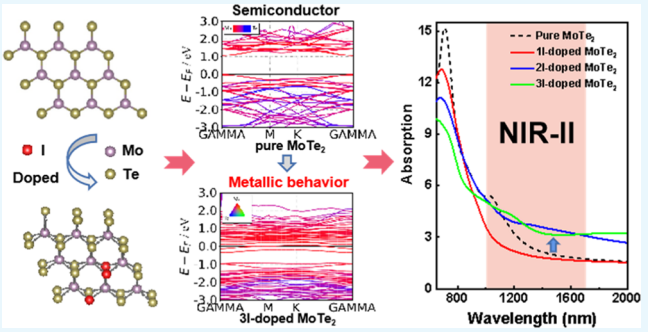

1. INTRODUCTION

In recent years, near-infrared fluorescence imaging technology has played an important role in applications such as biological imaging,[1−4] drug distribution tracking,[5,6] disease diagnosis,[7,8] and tumor imaging.[9,10] Compared with routine imaging technologies including computed tomography (CT),[11] positron emission tomography (PET),[12] single-photon emission computed tomography (SPECT),[13] magnetic resonance imaging (MRI),[14] and ultrasound imaging,[15] the greatest advantage of NIR fluorescence imaging is its high spatial resolution due to the reduced photon scattering, light absorption, and autofluorescence background.[16] In general, photon scattering intensity decays exponentially with increasing wavelengths; compared with visible light (400−700 nm) and near-infrared I (NIR-I, 700−900 nm), NIR-II (1000−1700 nm) can provide the highest spatial-temporal resolution with the lowest autofluorescence and deepest penetration, which has attracted much attention in the potential diagnosis.[17−19]

To date, materials such as carbon nanotubes,[20,21] quantum dots,[22,23] rare earth,[24,25] gold clusters,[9,26] polymers,[27] and small molecules[28,29] have exhibited excellent NIR-II fluorescence. Rare earth nanoparticles represented by lanthanide compounds, as the new generation of NIR fluorescent nanoprobes, have recently aroused enormous interest in biological imaging applications owing to their unique properties of low photobleaching, long luminescence lifetime, and narrow emission width.[30−32] However, lanthanide compounds may not be the answer to NIR-II imaging, considering their relatively low quantum yield and it is still important to explore other types of materials. The wavelength of NIR-II (1000−1700 nm) corresponds to 0.73−1.24 eV, which leads to the natural band gap of 2D materials. Band-gap engineering is a powerful technique to adjust the properties of 2D materials.[33,34] Accordingly, continuous efforts such as doping have been devoted to finding semiconductor materials with appropriate optical properties, which are indicated by their band gaps.

As an important member of 2D transition metal dichalcogenides (TMDs) with unique optical and electronic properties, $MoTe_2$ is an indirect band-gap semiconductor with an optical gap of approximately 1.0 eV.[35−37] As the thickness of bulk $MoTe_2$ reduced to a monolayer (1.1 eV), some special phenomena such as the mutual conversion between the indirect and direct band gap can be observed,[38,39] which

Received: January 5, 2022
Accepted: March 15, 2022
Published: March 29, 2022

provides an attractive direction for adjusting the properties of materials on demand. For example, Kanoun et al. demonstrated that transition metal atoms such as V-, Cr-, Mn-, Fe-, and Co-doped monolayer $MoTe_2$ can induce magnetic moment due to strong p−d hybridization between 5p states of Te atoms and 4d states of Mo atoms.[40] In addition, 3d and 4d transition metal atom-doped $MoTe_2$ has been studied by Kumar et al., indicating that doping can be used to tune the phase transition in $MoTe_2$.[41] In the research presented by Liu et al., the impurity level induced by the strong hybridization between the Te 5p and Au 5d orbitals crosses the Fermi level, making the Au-doped monolayer $MoTe_2$ system exhibit metallic behavior with 0 band gap.[42]

At present, researchers have done some research on monolayer $MoTe_2$ and achieved some research results, but there are still few studies on the optical properties of monolayer $MoTe_2$, especially in the NIR-II. Considering the potential NIR-II applications and band-gap engineering, the halogen I atom is an excellent candidate dopant to improve the electronic and optical properties of materials. Recently, Tang et al. simulated the enhancement of visible light absorption of pristine BiOCl by band-gap engineering (the substitutional I doping at the Cl site) due to the electronegativity difference between Cl and I atoms.[43] Kutlu et al. found that the band structure of the I atom-doped monolayer black phosphorus (BP) system was spin-dependent, where the source of the spin state was mainly the p orbital of the I atom. Moreover, the absorption of low-energy regions was improved to some extent after doping.[44] Wang et al. reported that I doping induced a slight band-gap reduction in the 2D metal-phthalocyanine-based pyrazine-linked conjugated covalent organic framework (c-COF ZnPc-pz) system and improved its absorption intensity in the NIR region, which was attributed to the interaction between the electron donor (ZnPc-pz) and acceptor (I_2) in ZnPc-pz-I_2.[45]

In this work, the electronic and optical properties of I-doped $MoTe_2$ systems with different I concentrations were systematically studied using first-principles simulations. The results show that I incorporation leads to bandwidth reduction. Meanwhile, n-type doping is identified in the doped systems exhibiting metallic behavior. The optical absorption capacity of the doped systems in the NIR-II window was significantly improved with an increase in the I doping concentration, which indicated that the substitutional I doping can optimize the electronic structure and broaden the potential application fields of $MoTe_2$.

2. SIMULATION DETAILS

The electronic and optical properties of pure and I-doped monolayer $MoTe_2$ have been investigated with the Vienna Ab initio Simulation Package (VASP) code, which is based on the framework of density functional theory (DFT).[46−48] The Perdew−Burke−Ernzerhof (PBE) functional, one of the most famous generalized gradient approximation (GGA) functionals is employed to describe the exchange−correlation potential.[49] The projector augmented wave (PAW)[50,51] is utilized to describe the electron−ion interactions with $4d^5 5s^1$ and $5s^2 5p^4$ as the valence-electron configurations of Mo and Te atoms, respectively. The calculations are carried out at a constant volume, and the adopted monolayer structure is a 3 × 3 × 1 $MoTe_2$ supercell containing 9 Mo atoms and 18 Te atoms, which is sufficient for the simulations: binding energies of different substituted configurations for doped $MoTe_2$ with 3 × 3 × 1 and relatively large 4 × 4 × 1 supercells are converged (see Table S1 for details). Binding energies of each substitution doping configuration are calculated according to the following expression

$$E_b = E_{doped} - E_{pure} + mE_{Te} - nE_I$$

where E_{doped} and E_{pure} are the total energies of I-doped and pure monolayer $MoTe_2$, respectively, m is the number of the removed Te atoms, n is the number of I atoms that are doped in the system, and E_{Te} and E_I are energy per atom for the Te and I dopant atoms, respectively.

To avoid the interaction between layers due to periodicity and improve the reliability and accuracy of calculations, a vacuum distance of 20 Å is taken along the z-direction perpendicular to the monolayer surface. In this paper, a substitution doping method is performed to replace Te atoms in monolayer $MoTe_2$ with one, two, and three I atoms. To ensure the convergence of calculations, the cutoff energy for the plane-wave basis is set to 450 eV. In addition, all Brillouin zone integrations are performed according to the Monkhorst Pack scheme,[52] a 5 × 5 × 1 k-mesh based on the Γ-centered scheme for relaxation calculations. For structural relaxation, the convergence criteria for energy and force are set to 1×10^{-6} eV and −0.01 eV/Å, respectively. In this work, the Heyd−Scuseria−Ernzerhof (HSE06)[53] hybrid functional is also employed to verify the impact of HF exchange on the band gap and optical properties. The exchange−correlation energy in HSE06 is then defined as

$$E_{xc}^{HSE} = aE_x^{HF,SR}(\omega) + (1-a)E_x^{PBE,SR}(\omega) + E_x^{PBE,LR}(\omega) + E_c^{PBE}$$

where $E_x^{HF,SR}$ is the short-range HF exchange, $E_x^{PBE,SR}$ and $E_x^{PBE,LR}$ are the short-range and long-range components of the PBE exchange functional obtained by integration of the model PBE exchange hole,[54,55] and E_c^{PBE} is the correlation energy. In the HSE calculations, the mixing parameter is set to the standard value of $\alpha = 0.25$ and the HF screening parameter μ is set to 0.2 $Å^{-1}$.

In the random phase approximation (RPA),[56] local field effects are neglected. The optical properties of semiconductors in the linear response range are generally described by the dielectric function $\varepsilon(\omega)$

$$\varepsilon(\omega) = \varepsilon_1(\omega) + \varepsilon_2(\omega)$$

where $\varepsilon_1(\omega)$ and $\varepsilon_2(\omega)$ are the real and imaginary parts of the dielectric function, respectively, and ω is the frequency of electromagnetic waves. The imaginary part of the dielectric function $\varepsilon_2(\omega)$ reflects the absorption of photons by the system, which is calculated by the transition of valence electrons between occupied and unoccupied orbits.[57]

3. RESULTS AND DISCUSSION

To set up valid models of doped monolayer $MoTe_2$, different possibilities are explored and evaluated. According to different stacking modes, monolayer $MoTe_2$ has three crystal phases, namely the semiconducting 2H phase, the metallic 1T phase, and the semimetallic distorted octahedral 1T′ phase, respectively.[58−60] The 2H phase, which is commonly studied is the most stable form among the three crystal structures.[61] Monolayer $MoTe_2$ is composed of hexagonally arranged Mo atoms that are sandwiched between two layers of Te atoms with schematic illustrations of top and side views shown in

https://doi.org/10.1021/acsomega.2c00071
ACS Omega 2022, 7, 11956−11963

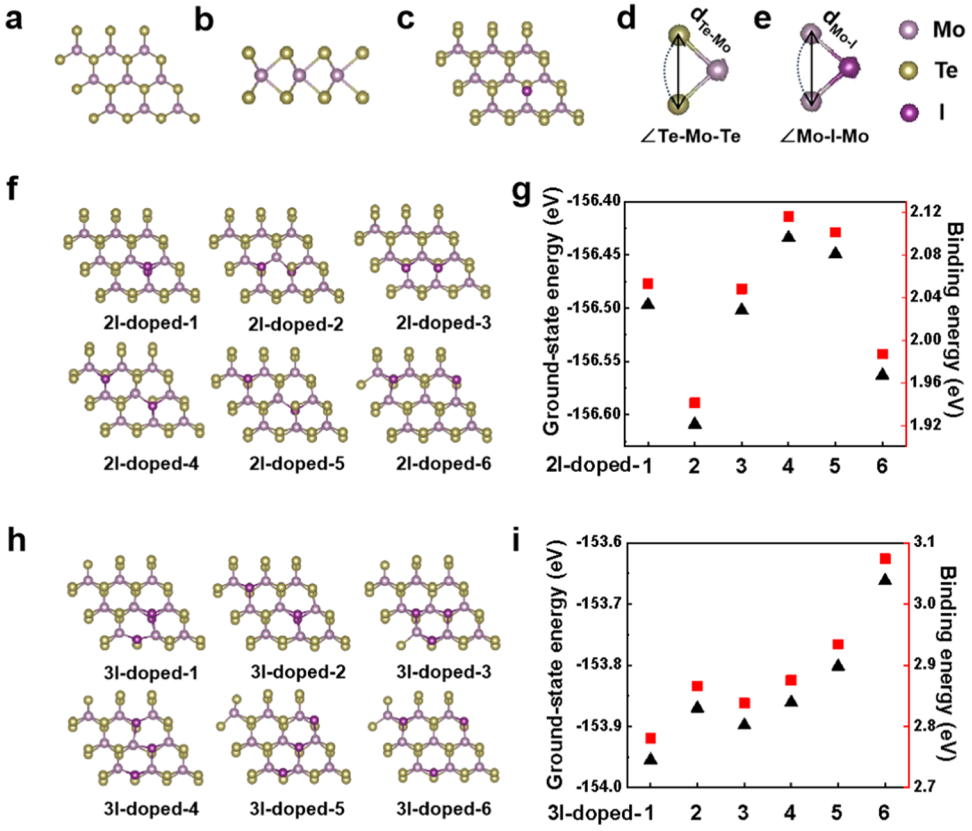

Figure 1. (a) Top and (b) side views of the monolayer $MoTe_2$. (c) Atomic structure of the single I atom doped with monolayer $MoTe_2$. (d) Schematic diagram of the distance between Te and Mo atoms (d_{Te-Mo}) and the angle of the Te−Mo bond (∠Te−Mo−Te). (e) Schematic diagram of the distance between Mo and I atoms (d_{Mo-I}) and the angle of the Mo−I bond (∠Mo−I−Mo). The pink, yellow, and purple balls represent Mo, Te, and I atoms. The top view of six different configurations of $MoTe_2$ systems doped with (f) two and (h) three I atoms, respectively. Comparison of the ground-state energies and binding energies for (g) two and (i) three I atom-doped $MoTe_2$.

Figure 1a,b, respectively. According to the substitutional doping method, Te atoms can be replaced by I atoms in $MoTe_2$. All configurations of $MoTe_2$ systems doped with one, two, and three I atoms per supercell are shown in Figure 1c,f,h, respectively. Binding energies and ground-state energies are used to screen the unphysical configurations. Simulation results show that the two I-doped $MoTe_2$-2 and three I-doped $MoTe_2$-1 exhibit the lowest ground-state energies and binding energies (Figure 1g,i). Thus, the two configurations are focused on in the simulations.

To gain more information on the structural changes caused by doping I atoms, the optimized geometric parameters of all doped systems are listed in Table 1; bond lengths are denoted d_{Te-Mo} and d_{I-Mo} and bond angles are denoted ∠Te−Mo−Te and ∠Mo−I−Mo, as shown in Figure 1d,e. Meanwhile, the geometric parameters of pure monolayer $MoTe_2$ are also listed for comparison. It can be seen that the lattice constant a of the optimized monolayer $MoTe_2$ is 3.553 Å, which is in good agreement with the previous experimental[62] and theoretical calculation results,[63] indicating that the calculation method is reasonable and the calculation results are reliable. In addition, it is found that the geometric parameters in the I-doped $MoTe_2$ systems are close to those in pure monolayer $MoTe_2$, which is attributed to the I and Te atoms in the same period having similar atomic radii.[64,65]

The transition from semiconducting to metallic behavior of I-doped $MoTe_2$ systems can be associated with the impurity level introduced by doping. As shown in Figure 2a, the band

Table 1. Calculated Lattice Constant a, Bond Lengths (d_{Te-Mo} and d_{I-Mo}), and Bond Angles (∠Te−Mo−Te and ∠Mo−I−Mo) of the Optimized $MoTe_2$ Systems Doped with Different I Atom Concentrations, Respectively, Together with Those of Pure Monolayer $MoTe_2$

configurations	lattice constant a (Å)	d_{Te-Mo} (Å)	d_{I-Mo} (Å)	∠Te−Mo−Te (deg)	∠Mo−I−Mo (deg)
pure $MoTe_2$	3.553	2.736		80.991	
1I-doped $MoTe_2$	3.566	2.741	2.777	81.741	82.354
2I-doped $MoTe_2$	3.542	2.734	2.758	81.481	79.880
3I-doped $MoTe_2$	3.676	2.755	2.775	84.289	88.714

structure of pure monolayer $MoTe_2$ shows that the direct band gap at the highly symmetric G point is about 1.083 eV, which is consistent with the previous calculation results[62,63] and in good agreement with the experimental values.[35,66] In contrast to the semiconductor behavior in the pure monolayer $MoTe_2$, I-doped $MoTe_2$ systems appear to exhibit metallic behavior (Figure 2b−d). Compared with the PBE results, the HSE calculations significantly overestimate the band gap of pure $MoTe_2$ by 50% (see Figure S1 and Table 2 for details). In the simulations, the nonlocal feature of the HF exchange may be insignificant and HSE06 may not be an appropriate functional to use. The energy bands of I-doped $MoTe_2$ systems are highly dense and show a significant shift to the lower energy area.

https://doi.org/10.1021/acsomega.2c00071
ACS Omega 2022, 7, 11956−11963

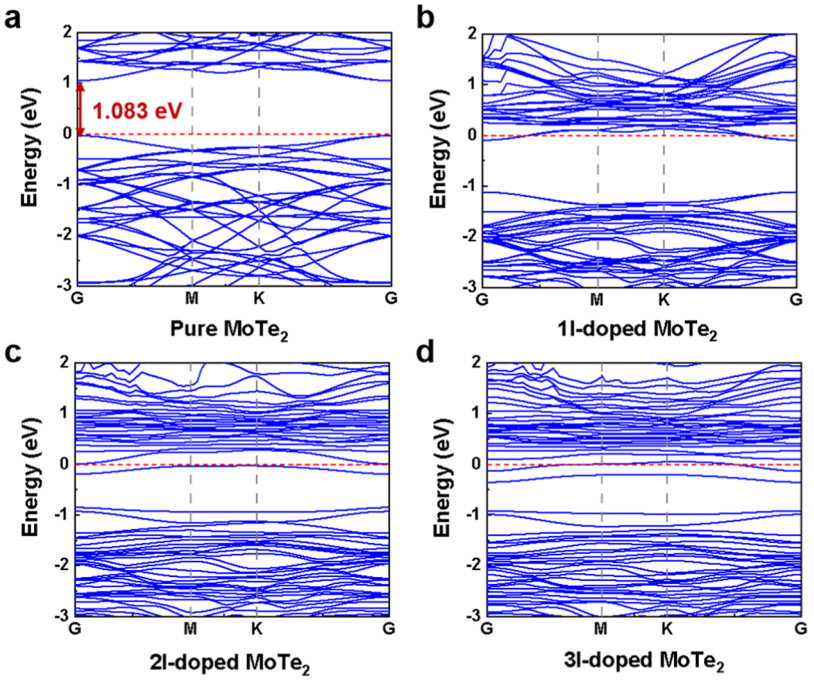

Figure 2. Band structures of (a) pure and (b–d) different I atom concentration-doped monolayer $MoTe_2$ calculated by the PBE method.

Table 2. Band Gap of Monolayer $MoTe_2$ (eV)

structures	PBE	HSE	experimental[35,66]	other theoretical studies[62,63]	
$MoTe_2$	1.083	1.509	1.10	1.07	1.10

Subsequently, impurity levels cross the Fermi level, making all doped systems exhibit metallic behavior, which is a typical characteristic of n-type doping.[67,68] In addition, with the increase in the I concentration, the bandwidth of I-doped $MoTe_2$ systems decreases due to the increase in the impurity level close to the Fermi level. As a result, each donor impurity removes a state from the conduction band and establishes it as an impurity level of lower energy in the interband. With the increasing concentration of impurity I atoms, the whole conduction band shifts down to a greater extent, and finally, impurity levels cross the Fermi level. Electrons in these impurity levels can conduct in the same way as electrons in metals, which increases the probability of electron transition near the Fermi level.

To further investigate the electronic properties, the total density of states (TDOS) and partial total density of states (PDOS) of pure and I-doped monolayer $MoTe_2$ are calculated, as shown in Figure 3. The DOS shows that impurity states produce highly localized orbitals within the band gap of the pure $MoTe_2$. In addition, the PDOS shows the electronic hybridization behavior among the Mo, Te, and I atoms. It can be found that the pure $MoTe_2$ valence band is mainly

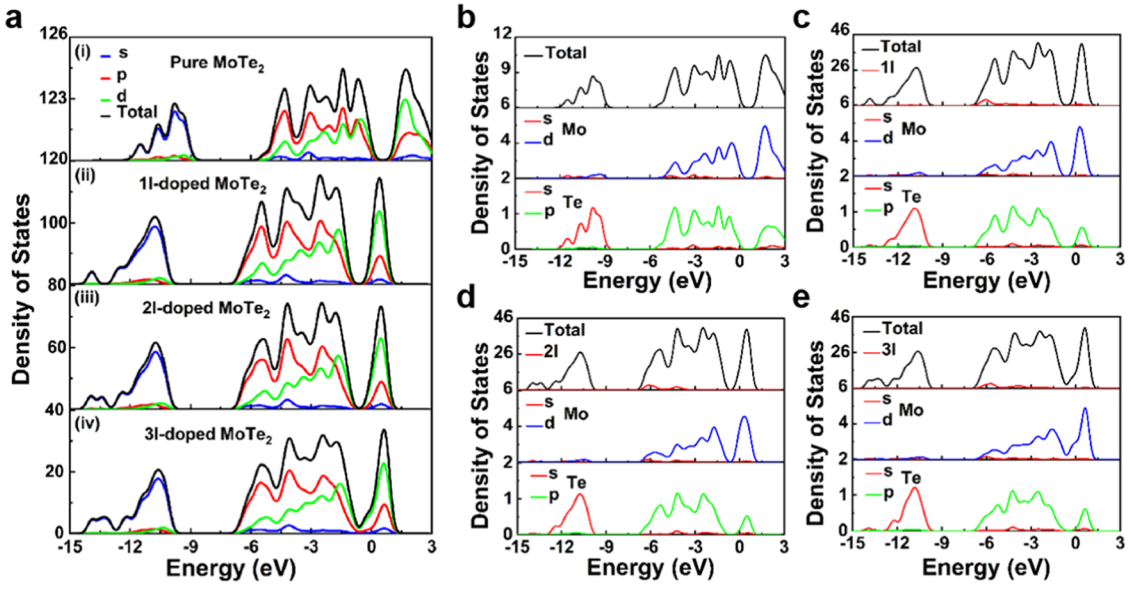

Figure 3. (a) TDOS and (b–e) PDOS of pure and different I atom concentration-doped monolayer $MoTe_2$.

https://doi.org/10.1021/acsomega.2c00071
ACS Omega 2022, 7, 11956−11963

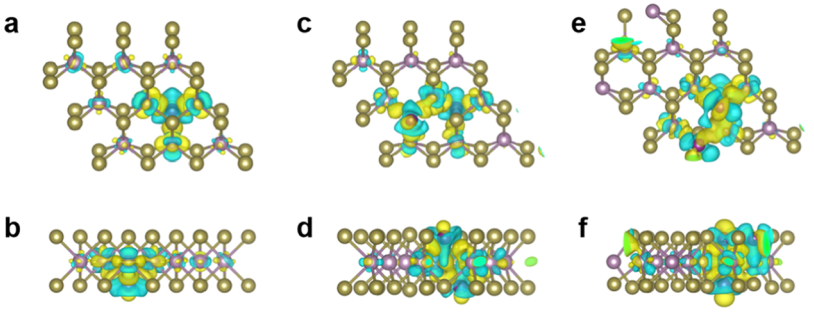

Figure 4. Top and side views of charge density differences of monolayer $MoTe_2$ doped with (a, b) one, (c, d) two, and (e, f) three I atoms, respectively. Isosurfaces correspond to 0.003 e $Å^{-3}$.

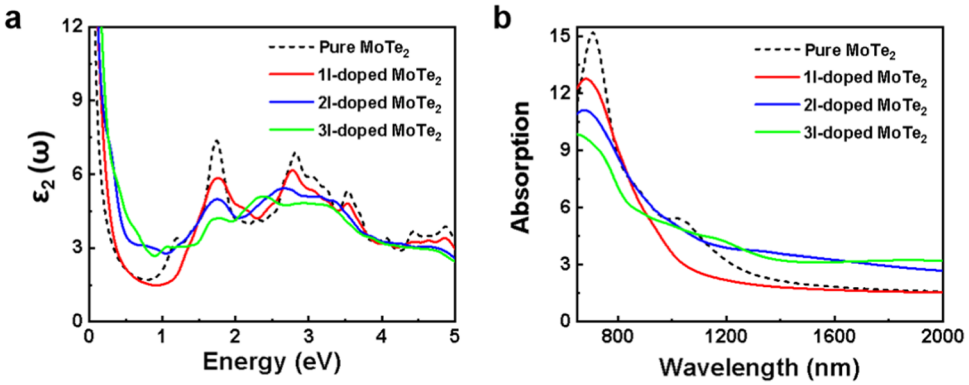

Figure 5. Optical properties of pure and different I atom concentration-doped monolayer $MoTe_2$ calculated by the PBE method: (a) imaginary part of the dielectric function $\varepsilon_2(\omega)$ and (b) absorption spectra.

composed of Te 5p and Mo 4d orbitals, while the conduction band is mainly composed of Mo 4d orbitals. The valence band shows the strong hybridization between Te 5p and Mo 4d orbitals with a bandwidth of approximately 6.0 eV. In addition, Te 5s states mainly emerge in the range of −12.5 to −8.4 eV, which is highly close to the band calculation results (Figure 3a(i),b). As shown in Figure 3a(ii)−(iv), I 5s states are observed in the energy range of −14.3 to −12.8 eV, which can be attributed to the strong localization of doped I atoms. Moreover, I 5s states are gradually enhanced with the increase in the I concentration. Figure 3b−e shows that Te 5s states have shifted slightly to the low-energy area after I doping. It should be noted that the number of Te atoms is decreased due to the substitution of I atoms, thus Te 5p states at the top of valence bands are slightly reduced. Upon I atom doping, both valence bands and conduction bands shift to the low-energy area; conduction bands are mainly composed of Mo 4d and Te 5p orbitals and valence bands are mainly dominated by Te 5p, Mo 4d, and I 5p orbitals, suggesting the possible interactions between the I and Te and Mo atoms. Specifically, 4d orbitals of Mo atoms in monolayer $MoTe_2$ were strongly hybridized with 5p orbitals of I dopants due to the large overlap, and impurity levels introduced by hybridization cross the Fermi level, implying metallic behavior of all doped systems. In addition, the DOS of I-doped $MoTe_2$ systems near the Fermi level is not zero, which may be due to the distribution of impurity levels induced by doping I atoms in the interband.

The charge density difference is calculated to investigate charge transfer between the I atoms and monolayer $MoTe_2$. Figure 4 displays the optimized stable configurations and their corresponding charge density differences for the doped systems. It can be seen that impurity atoms in the doped systems interact strongly with neighbor atoms and their charge distributions changed significantly. The yellow regions represent charge accumulation and the blue regions represent charge depletion. Interestingly, with the introduction of the I atom, the regions with strong bonding between I and Mo atoms are found in the I-doped $MoTe_2$ systems,[69] which may indicate the covalent interaction between I and neighbor Mo atoms (Figure 4a−f). In addition, there is charge depletion around the I atoms and charge accumulation near the Mo atoms in the doped systems, that is, the I atoms lose electrons and Mo atoms gain electrons, which are consistent with the orbital hybridization between Mo and I atoms in the PDOS. Therefore, the change in the global electronic properties of I-doped $MoTe_2$ systems is attributed to local changes in electron distribution.[70]

To better understand the optical transition of the doped systems, it is very imperative to investigate the imaginary part of dielectric function $\varepsilon_2(\omega)$. $\varepsilon_2(\omega)$ of pure and I-doped $MoTe_2$ is shown in Figure 5a. Due to the hexagonal symmetry of monolayer $MoTe_2$, $\varepsilon_2(\omega)$ exhibits obvious anisotropy. For pure $MoTe_2$, three distinct peaks are observed at 1.75, 2.82, and 3.53 eV. As a direct band-gap semiconductor, the spectrum of pure $MoTe_2$ is generated by the electronic transition between energy levels, and each dielectric peak can be explained by its band structure and PDOS. Combined with the PDOS in Figure 3b, it is found that the main peak at 1.75 eV is mainly due to the intrinsic transition between Te 5p states in the highest valence band and Mo 4d states in the lowest conduction band, while main peaks at the corresponding position in I-doped $MoTe_2$ systems are mainly derived from the electron transition among Mo 4d, I 5p, and Te 5p states. In addition, compared with pure $MoTe_2$, the three peaks

https://doi.org/10.1021/acsomega.2c00071
ACS Omega 2022, 7, 11956−11963

of all doped systems have significant red shifts, and the corresponding intensity decreases with the increase in the I doping concentration. The reason that the height of the main peak at 1.75 eV decreases with increasing I doping concentration is that the 5p orbitals of I increasingly occupy the dominant position in the energy band, which greatly reduces the probability of the electron hopping change process in the 4d state of Mo and the 5p state of Te. To sum up, these results imply that the bandwidth of I-doped $MoTe_2$ systems is reduced, which is related to the local lattice distortion of a pure $MoTe_2$ structure caused by the doping of impurity I atoms and the introduction of impurity levels in the doped systems. $\varepsilon_2(\omega)$ of pure $MoTe_2$ simulated using an HSE06 hybrid functional (Figure S2a) shows some new dielectric peaks, which are significantly deviated from the PBE simulation results. The HF exchange for simulating the optical properties of I-doped $MoTe_2$ systems seems to be inappropriate.

The simulations of absorption spectra suggest that a relatively high doping concentration can more effectively enhance the absorption ability of $MoTe_2$ in the NIR-II window. As shown in Figure 5b, compared with pure monolayer $MoTe_2$, the optical absorption of single I atom-doped $MoTe_2$ in the NIR-II window is very weak, while two and three I atom-doped $MoTe_2$ systems show considerable improvement in the NIR-II absorption. Specifically, the two I atom-doped $MoTe_2$ shows an absorption peak at 1300 nm, while the three I atom-doped $MoTe_2$ has an absorption peak at 1180 and an absorption enhancement at 1700 nm. The absorption amplitude of I-doped $MoTe_2$ systems in the NIR-II window is significantly enhanced. According to the previous theoretical work,[71] the emission spectrum is the product of the absorption spectrum and quasi-Fermi distributions for electrons and holes. The absorption spectra are enhanced in the NIR-II region by iodine doping. The quasi-Fermi distribution, which is the production of occupied conduction states and unoccupied valence states can be improved by the semiconductor−conductor conversion: in I-doped $MoTe_2$ systems, occupied conduction states and unoccupied valence states can be created much easier. Therefore, it can be inferred that the relatively high doping concentration can also improve emission in the NIR-II window. Among them, the absorption coefficient of the $MoTe_2$ system doped with three I atoms increases significantly, which is due to the introduction of more impurity levels in the interband and thus effortless transition for electrons from impurity levels to conduction bands.

4. CONCLUSIONS

In summary, first-principles calculations have been employed to investigate the electronic and optical properties of the $MoTe_2$ doped with different I concentrations. Compared with pure $MoTe_2$, the bandwidth of I-doped $MoTe_2$ systems decreases with increasing I doping. In addition, all doped systems show metallic properties because impurity levels induced by I doping cross the Fermi level. According to the analysis of optical properties, with the increase in the I doping concentration, the absorption amplitude of the doped systems in the NIR-II region is significantly improved and the quasi-Fermi distribution can also be improved, thus the emission spectra, which are the product of the absorption spectra and quasi-Fermi distributions for electrons and holes can be enhanced in the NIR-II window.

The theoretical simulation including the band structure and DOS may represent the actual electron structure due to the convergence between the simulated band gap and the experimental band gap of $MoTe_2$. The first-principles algorithms do not reproduce the fluorescence characters at the theory level. Kasha's rule[72] provides a bottom line of the link between absorption and emission but the details of fluorescence including the molecular oscillations in the emission process are still unclear. This work shows the potential of NIR-II emission materials, I-doped $MoTe_2$. Experimental synthesis and measurements are needed to confirm the effectiveness of the emission in the future.

■ ASSOCIATED CONTENT

Supporting Information

The Supporting Information is available free of charge at https://pubs.acs.org/doi/10.1021/acsomega.2c00071.

Band structures, imaginary part of the dielectric function $\varepsilon_2(\omega)$, and absorption spectra of pure and different I atom concentration-doped monolayer $MoTe_2$ calculated by the HSE06 functional and binding energies of different substituted configurations for doped $MoTe_2$ with $3 \times 3 \times 1$ and relatively large $4 \times 4 \times 1$ supercells (PDF)

■ AUTHOR INFORMATION

Corresponding Authors

Ling Liu − *Tianjin Key Laboratory of Brain Science and Neural Engineering, Academy of Medical Engineering and Translational Medicine, Tianjin University, Tianjin 300072, China; Department of Physics, Shanxi Medical University, Taiyuan 030001, China*; Email: liugoupan@163.com

Yonghui Li − *Department of Physics and Tianjin Key Laboratory of Low Dimensional Materials Physics and Preparing Technology, Institute of Advanced Materials Physics, School of Sciences, Tianjin University, Tianjin 300350, China*; Email: yonghui.li@tju.edu.cn

Xiao-Dong Zhang − *Tianjin Key Laboratory of Brain Science and Neural Engineering, Academy of Medical Engineering and Translational Medicine, Tianjin University, Tianjin 300072, China; Department of Physics and Tianjin Key Laboratory of Low Dimensional Materials Physics and Preparing Technology, Institute of Advanced Materials Physics, School of Sciences, Tianjin University, Tianjin 300350, China*; orcid.org/0000-0002-7212-0138; Email: xiaodongzhang@tju.edu.cn

Authors

Yue Zhao − *Tianjin Key Laboratory of Brain Science and Neural Engineering, Academy of Medical Engineering and Translational Medicine, Tianjin University, Tianjin 300072, China*

Shuangjie Liu − *Tianjin Key Laboratory of Brain Science and Neural Engineering, Academy of Medical Engineering and Translational Medicine, Tianjin University, Tianjin 300072, China*

Yang Wang − *Tianjin Key Laboratory of Brain Science and Neural Engineering, Academy of Medical Engineering and Translational Medicine, Tianjin University, Tianjin 300072, China*

Complete contact information is available at: https://pubs.acs.org/10.1021/acsomega.2c00071

https://doi.org/10.1021/acsomega.2c00071
ACS Omega 2022, 7, 11956−11963

Notes

The authors declare no competing financial interest.

■ ACKNOWLEDGMENTS

This work was financially supported by the National Natural Science Foundation of China (Grant Nos. 91859101, 81971744, U1932107, 82001952, and 11804248), the National Key Research and Development Program of China (2021YFF1200030), the Outstanding Youth Funds of Tianjin, the National Natural Science Foundation of Tianjin (Nos. 19JCZDJC34000 and 20JCYBJC00940), the Innovation Foundation of Tianjin University, and the CAS Interdisciplinary Innovation Team (JCTD-2020-08).

■ REFERENCES

(1) Hong, G.; Antaris, A. L.; Dai, H. Near-infrared fluorophores for biomedical imaging. *Nat. Biomed. Eng.* **2017**, *1*, No. 0010.
(2) Wan, H.; Yue, J.; Zhu, S.; Uno, T.; Zhang, X.; Yang, Q.; Yu, K.; Hong, G.; Wang, J.; Li, L.; et al. A bright organic NIR-II nanofluorophore for three-dimensional imaging into biological tissues. *Nat. Commun.* **2018**, *9*, No. 1171.
(3) Wang, H.; Mu, X.; Yang, J.; Liang, Y.; Zhang, X.-D.; Ming, D. Brain imaging with near-infrared fluorophores. *Coord. Chem. Rev.* **2019**, *380*, 550−571.
(4) Diao, S.; Hong, G.; Antaris, A. L.; Blackburn, J. L.; Cheng, K.; Cheng, Z.; Dai, H. Biological imaging without autofluorescence in the second near-infrared region. *Nano. Res.* **2015**, *8*, 3027−3034.
(5) Lv, C.; Zhang, T. Y.; Lin, Y.; Tang, M.; Zhai, C. H.; Xia, H. F.; Wang, J.; Zhang, Z. L.; Xie, Z. X.; Chen, G.; et al. Transformation of Viral Light Particles into Near-Infrared Fluorescence Quantum Dot-Labeled Active Tumor-Targeting Nanovectors for Drug Delivery. *Nano Lett.* **2019**, *19*, 7035−7042.
(6) Fan, Z.; Chang, Y.; Cui, C.; Sun, L.; Wang, D. H.; Pan, Z.; Zhang, M. Near infrared fluorescent peptide nanoparticles for enhancing esophageal cancer therapeutic efficacy. *Nat. Commun.* **2018**, *9*, No. 2605.
(7) Huang, J.; Pu, K. Near-infrared fluorescent molecular probes for imaging and diagnosis of nephro-urological diseases. *Chem. Sci.* **2021**, *12*, 3379−3392.
(8) Huang, J.; Jiang, Y.; Li, J.; He, S.; Huang, J.; Pu, K. A Renal-Clearable Macromolecular Reporter for Near-Infrared Fluorescence Imaging of Bladder Cancer. *Angew. Chem., Int. Ed.* **2020**, *59*, 4415−4420.
(9) Liu, H.; Hong, G.; Luo, Z.; Chen, J.; Chang, J.; Gong, M.; He, H.; Yang, J.; Yuan, X.; Li, L.; et al. Atomic-Precision Gold Clusters for NIR-II Imaging. *Adv. Mater.* **2019**, *31*, No. e1901015.
(10) van Dam, G. M.; Crane, L.; Harlaar, N. J.; Ntziachristos, V.; et al. Intraoperative tumor-specific fluorescence imaging in ovarian cancer by folate receptor-alpha targeting: First in-human results. *Nat. Med.* **2011**, *17*, 1315−1319.
(11) Galperin, A.; Margel, D.; Baniel, J.; Dank, G.; Biton, H.; Margel, S. Radiopaque iodinated polymeric nanoparticles for X-ray imaging applications. *Biomaterials* **2007**, *28*, 4461−4468.
(12) Yamashita, S.; Takashima, T.; Kataoka, M.; Oh, H.; Watanabe, Y.; et al. PET imaging of the gastrointestinal absorption of orally administered drugs in conscious and anesthetized rats. *J. Nucl. Med.* **2011**, *52*, 249−256.
(13) Merkel, O. M.; Librizzi, D.; Pfestroff, A.; Schurrat, T.; BeHe, M.; Kissel, T. In Vivo SPECT and Real-Time Gamma Camera Imaging of Biodistribution and Pharmacokinetics of siRNA Delivery Using an Optimized Radiolabeling and Purification Procedure. *Bioconjugate Chem.* **2009**, *20*, 174−182.
(14) Zhou, Z.; Yang, L.; Gao, J.; Chen, X. Structure-Relaxivity Relationships of Magnetic Nanoparticles for Magnetic Resonance Imaging. *Adv. Mater.* **2019**, *31*, No. e1804567.
(15) Sebag, F.; Vaillant-Lombard, J.; Berbis, J.; Griset, V.; Henry, J. F.; Petit, P.; Oliver, C. Shear Wave Elastography: A New Ultrasound Imaging Mode for the Differential Diagnosis of Benign and Malignant Thyroid Nodules. *J. Clin. Endocrinol. Metab.* **2010**, *95*, 5281−5288.
(16) Cao, J.; Zhu, B.; Zheng, K.; He, S.; Yang, H.; et al. Recent Progress in NIR-II Contrast Agent for Biological Imaging. *Front. Bioeng. Biotechnol.* **2020**, *7*, No. 487.
(17) Hong, G. L.; J, C.; Robinson, J. T.; Raaz, U.; Xie, L.; Huang, N. F.; Cooke, J. P.; Dai, H. Multifunctional in vivo vascular imaging using near-infrared II fluorescence. *Nat. Med.* **2012**, *18*, 1841−1846.
(18) Wan, H.; Du, H.; Wang, F.; Dai, H. Molecular imaging in the second near-infrared window. *Adv. Funct. Mater.* **2019**, *29*, No. 1900566.
(19) Ma, H.; Wang, J.; Zhang, X.-D. Near-infrared II emissive metal clusters: From atom physics to biomedicine. *Coord. Chem. Rev.* **2021**, *448*, No. 214184.
(20) Hong, G.; Diao, S.; Chang, J.; Antaris, A. L.; Chen, C.; Zhang, B.; Zhao, S.; Atochin, D. N.; Huang, P. L.; Andreasson, K. I.; et al. Through Skull Fluorescence Imaging of the Brain in a New Near-Infrared Window. *Nat. Photonics* **2014**, *8*, 723−730.
(21) Liang, C.; Diao, S.; Wang, C.; Gong, H.; Liu, T.; Hong, G.; Shi, X.; Dai, H.; Liu, Z. Tumor metastasis inhibition by imaging-guided photothermal therapy with single-walled carbon nanotubes. *Adv. Mater.* **2014**, *26*, 5646−5652.
(22) Zhang, M. Y.J.; Ran, C.; Ma, Z.; Dai, H.; et al. Bright quantum dots emitting at 1,600 nm in the NIR-IIb window for deep tissue fluorescence imaging. *Proc. Nat. Acad. Sci. U.S.A.* **2018**, *115*, 6590−6595.
(23) Zebibula, A.; Alifu, N.; Xia, L.; Sun, C.; Yu, X.; Xue, D.; Liu, L.; Li, G.; Qian, J. Ultrastable and Biocompatible NIR-II Quantum Dots for Functional Bioimaging. *Adv. Funct. Mater.* **2018**, *28*, No. 1703451.
(24) Zhong, Y. M.Z.; Zhu, S.; Yue, J.; Zhang, M.; Antaris, A. L.; Yuan, J.; Cui, R.; Wan, H.; Zhou, Y.; et al. Boosting the down-shifting luminescence of rare-earth nanocrystals for biological imaging beyond 1500 nm. *Nat. Commun.* **2017**, *8*, No. 737.
(25) Zhong, Y.; Ma, Z.; Wang, F.; Wang, X.; Yang, Y.; Liu, Y.; Zhao, X.; Li, J.; Du, H.; Zhang, M.; et al. In vivo molecular imaging for immunotherapy using ultra-bright near-infrared-IIb rare-earth nanoparticles. *Nat. Biotechnol.* **2019**, *37*, 1322−1331.
(26) Chen, Y. M.; D, M.; Wei, H.; Cordero, J. M.; Schneider, M.; Guével, X.; Chen, O.; Bruns, O. T.; Bawendi, M. G. Shortwave Infrared in Vivo Imaging with Gold Nanoclusters. *Nano Lett.* **2017**, *17*, 6330−6334.
(27) Hong, G.; Zou, Y.; Antaris, A. L.; Diao, S.; Wu, D.; Cheng, K.; Zhang, X.; Chen, C.; Liu, B.; He, Y.; et al. Ultrafast fluorescence imaging in vivo with conjugated polymer fluorophores in the second near-infrared window. *Nat. Commun.* **2014**, *5*, No. 4206.
(28) Antaris, A. L.; Chen, H.; Cheng, K.; Sun, Y.; Hong, G.; Qu, C.; Diao, S.; Deng, Z.; Hu, X.; Zhang, B.; et al. A small-molecule dye for NIR-II imaging. *Nat. Mater.* **2016**, *15*, 235−242.
(29) Zhang, X. D.; Wang, H.; Antaris, A. L.; Li, L.; Diao, S.; Ma, R.; Nguyen, A.; Hong, G.; Ma, Z.; Wang, J.; et al. Traumatic Brain Injury Imaging in the Second Near-Infrared Window with a Molecular Fluorophore. *Adv. Mater.* **2016**, *28*, 6872−6879.
(30) Yang, Y.; Tu, D.; Zhang, Y.; Zhang, P.; Chen, X. Recent Advances in Design of Lanthanide-Containing NIR-II Luminescent Nanoprobes. *iScience* **2021**, *24*, No. 102062.
(31) Fan, Y.; Zhang, F. A New Generation of NIR-II Probes: Lanthanide-Based Nanocrystals for Bioimaging and Biosensing. *Adv. Opt. Mater.* **2019**, *7*, No. 1801417.
(32) Ning, Y.; Zhu, M.; Zhang, J. L. Near-infrared (NIR) lanthanide molecular probes for bioimaging and biosensing. *Coord. Chem. Rev.* **2019**, *399*, No. 213028.
(33) Kang, M.; Kim, B.; Ryu, S. H.; Jung, S. W.; Kim, J.; Moreschini, L.; Jozwiak, C.; Rotenberg, E.; Bostwick, A.; Kim, K. S. Universal Mechanism of Band-Gap Engineering in Transition-Metal Dichalcogenides. *Nano Lett.* **2017**, *17*, 1610−1615.
(34) Capasso, F. Band-gap engineering: from physics and materials to new semiconductor devices. *Science* **1987**, *235*, 172−176.

https://doi.org/10.1021/acsomega.2c00071
ACS Omega 2022, 7, 11956−11963

(35) Ruppert, C.; Aslan, O. B.; Heinz, T. F. Optical properties and band gap of single- and few-layer $MoTe_2$ crystals. *Nano Lett.* **2014**, *14*, 6231−6236.
(36) Yamamoto, M.; Wang, S. T.; Ni, M.; Lin, Y. F.; Li, S. L.; Aikawa, S.; Jian, W. B.; Ueno, K.; Waka Ba Yashi, K.; Tsukagoshi, K. Strong Enhancement of Raman Scattering from a Bulk-Inactive Vibrational Mode in Few-Layer $MoTe_2$. *ACS Nano* **2014**, *8*, 3895−3903.
(37) Mendioroz, R. Z.; Sopha, H.; Charvot, J.; Krumpolec, R.; Rodriguez-Pereira, J.; Michalika, J.; Mistrík, J.; Baa, D.; Motola, M.; Bure, F. 2D $MoTe_2$ nanosheets by atomic layer deposition: Excellent photo-electrocatalytic properties. *Appl. Mater. Today* **2021**, *23*, No. 101017.
(38) Cao, M.; Ni, L.; Wang, Z.; Liu, J.; Duan, L.; et al. DFT Investigation on Direct Z-scheme Photocatalyst for Overall Water Splitting: $MoTe_2$/BAs van der Waals Heterostructure. *Appl. Surf. Sci.* **2021**, *551*, No. 149364.
(39) Lezama, I. G.; Arora, A.; U Ba Ldini, A.; Ba Rreteau, C.; Morpurgo, A. F.; et al. Indirect-to-Direct Band Gap Crossover in Few-Layer $MoTe_2$. *Nano Lett.* **2015**, *15*, 2336−2342.
(40) Kanoun, M. B. Tuning magnetic properties of two-dimensional $MoTe_2$ monolayer by doping 3d transition metals: Insights from first principles calculations. *J. Alloys Compd.* **2018**, *748*, 938−942.
(41) Kumar, A.; Strachan, A.; Onofrio, N. Prediction of low energy phase transition in metal doped $MoTe_2$ from first principle calculations. *J. Appl. Phys.* **2019**, *125*, No. 204303.
(42) Liu, Y.; Shi, T.; Si, Q.; Liu, T. Adsorption and sensing performances of transition metal (Pd, Pt, Ag and Au) doped $MoTe_2$ monolayer upon NO_2: A DFT study. *Phys. Lett. A* **2020**, *391*, No. 127117.
(43) Zhang, L.; Tang, Z. K.; Lau, W. M.; Yin, W. J.; Hu, S. X.; Liu, L. M. Tuning band gaps and optical absorption of BiOCl through doping and strain: insight form DFT calculations. *Phys. Chem. Chem. Phys.* **2017**, *19*, 20968−20973.
(44) Kutlu, E.; Narin, P.; Lisesivdin, S. B.; Ozbay, E. Electronic and optical properties of black phosphorus doped with Au, Sn and I atoms. *Philos. Mag.* **2018**, *98*, 155−164.
(45) Wang, M.; Wang, M.; Lin, H. H.; Ballabio, M.; Feng, X.; et al. High-Mobility Semiconducting Two-Dimensional Conjugated Covalent Organic Frameworks with p-Type Doping. *J. Am. Chem. Soc.* **2020**, *142*, 21622−21627.
(46) Kresse, G. G. F.; J, J. Efficient Iterative Schemes for Ab Initio Total-Energy Calculations Using a Plane-Wave Basis Set. *Phys. Rev. B* **1996**, *54*, 11169−11186.
(47) Kresse, G.; Furthmüller, J. Efficiency of ab-initio total energy calculations for metals and semiconductors using a plane-wave basis set-ScienceDirect. *Comput. Mater. Sci.* **1996**, *6*, 15−50.
(48) Liu, H.; Li, Y.; Sun, S.; Xin, Q.; Zhang, X. D.; et al. Catalytically potent and selective clusterzymes for modulation of neuroinflammation through single-atom substitutions. *Nat. Commun.* **2021**, *12*, No. 114.
(49) Perdew, J. P.; Burke, K.; Ernzerhof, M. Generalized Gradient Approximation Made Simple. *Phys. Rev. Lett.* **1996**, *77*, 3865−3868.
(50) Blöchl, P. E. Projector augmented-wave method. *Phys. Rev. B* **1994**, *50*, 17953−17979.
(51) Kohn, W.; Sham, L. J. Self-Consistent Equations Including Exchange and Correlation Effects. *Phys. Rev. B* **1965**, *140*, A1133−A1138.
(52) Monkhorst, H. J.; Pack, J. D. Special points for Brillouin-zone integrations. *Phys. Rev. B* **1976**, *13*, 5188.
(53) Krukau, A. V.; Vydrov, O. A.; Izmaylov, A. F.; Scuseria, G. E. Influence of the exchange screening parameter on the performance of screened hybrid functionals. *J. Chem. Phys.* **2006**, *125*, No. 224106.
(54) Heyd, J.; Scuseria, G. E. Assessment and validation of a screened Coulomb hybrid density functional. *J. Chem. Phys.* **2004**, *120*, 7274−7280.
(55) Ernzerhof, M.; Perdew, J. P. Generalized gradient approximation to the angle- and system-averaged exchange hole. *J. Chem. Phys.* **1998**, *109*, 3313−3320.
(56) Ehrenreich, H.; Cohen, M. H. Self-Consistent Field Approach to the Many-Electron Problem. *Phys. Rev.* **1959**, *115*, 786−790.
(57) Zhang, X.; Guo, D.; M, L.; Liu, C.; L, W. Electronic and optical properties of $Ti_{1-x}Cd_xO_2$: A first-principles prediction. *Appl. Phys. Lett.* **2008**, *93*, No. 021103.
(58) Chhowalla, M.; Shin, H. S.; Eda, G.; Li, L. J.; Loh, K. P.; Hua, Z. The Chemistry of Two-Dimensional Layered Transition Metal Dichalcogenide Nanosheets. *Nat. Chem.* **2013**, *5*, 263−275.
(59) Zhang, C.; Santosh, K. C.; Nie, Y.; Liang, C.; Cho, K.; et al. Charge Mediated Reversible Metal-Insulator Transition in Monolayer $MoTe_2$ and $WxMo_{1-x}Te_2$ Alloy. *ACS Nano* **2016**, *10*, 7370−7375.
(60) Santosh, K. C.; Zhang, C.; Hong, S.; Wallace, R. M.; Cho, K. Phase stability of transition metal dichalcogenide by competing ligand field stabilization and charge density wave. *2D Mater.* **2015**, *2*, No. 035019.
(61) Wang, Y.; Xiao, J.; Zhu, H.; Li, Y.; Alsaid, Y.; Fong, K. Y.; Zhou, Y.; Wang, S.; Shi, W.; Wang, Y.; et al. Structural phase transition in monolayer $MoTe_2$ driven by electrostatic doping. *Nature* **2017**, *550*, 487−491.
(62) Chang, J.; Register, L. F.; Banerjee, S. K. Ballistic performance comparison of monolayer transition metal dichalcogenide MX_2 (M = Mo, W; X = S, Se, Te) metal-oxide-semiconductor field effect transistors. *J. Appl. Phys.* **2014**, *115*, No. 084506.
(63) Ma, Y.; Dai, Y.; Guo, M.; Niu, C.; Lu, J.; Huang, B. Electronic and magnetic properties of perfect, vacancy-doped, and nonmetal adsorbed $MoSe_2$, $MoTe_2$ and WS_2 monolayers. *Phys. Chem. Chem. Phys.* **2011**, *13*, 15546−15553.
(64) Cao, W.; Zhao, Q.; Yang, L.; Cui, H. Enhanced NO_x adsorption and sensing properties of $MoTe_2$ monolayer by Ni-doping: A first-principles study. *Surf. Interfaces* **2021**, *26*, No. 101372.
(65) Yu, W.; Zhu, Z.; Niu, C. Y.; Li, C.; Cho, J. H.; Jia, Y. Anomalous doping effect in black phosphorene using first-principles calculations. *Phys. Chem. Chem. Phys.* **2015**, *17*, 16351−16358.
(66) Xu, X.; Li, X.; Liu, K.; Li, J.; Feng, Q.; Zhou, L.; Cui, F.; Liang, X.; Lei, Z.; Liu, Z.; et al. Thermodynamics and Kinetics Synergetic Phase-Engineering of Chemical Vapor Deposition Grown Single Crystal $MoTe_2$ Nanosheets. *J. Cryst. Growth* **2018**, *18*, 2844−2850.
(67) Yang, C.; Zhao, X.; Wang, T.; Wei, S. Characters of group V and VII atoms doped WSe_2 monolayer. *J. Alloys Compd.* **2017**, *699*, 291−296.
(68) Zhao, X.; Xia, C.; Wang, T.; Peng, Y.; Dai, X. Effective p-type N-doped WS_2 monolayer. *J. Alloys Compd.* **2015**, *649*, 357−361.
(69) Hashmi, A.; Hong, J. Transition Metal Doped Phosphorene: First-Principles Study. *J. Phys. Chem. C* **2015**, *119*, 9198−9204.
(70) Zhao, Y.; Wang, W.; Li, C.; He, L. First-principles study of nonmetal doped monolayer $MoSe_2$ for tunable electronic and photocatalytic properties. *Sci. Rep.* **2017**, *7*, No. 17088.
(71) Bhattacharya, R.; et al. On conversion of luminescence into absorption and the van Roosbroeck-Shockley relation. *Appl. Phys. Lett.* **2012**, *100*, No. 222103.
(72) Kasha; Michael. Characterization of electronic transitions in complex molecules. *Discuss. Faraday Soc.* **1950**, *9*, 14−19.

https://doi.org/10.1021/acsomega.2c00071
ACS Omega 2022, 7, 11956−11963